

Cite this: DOI: 00.0000/xxxxxxxxxx

Voxel based method for predictive modelling of solidification and stress in digital light processing based additive manufacture[†]

Andrew Reid,^{*a} Joseph C Jackson,^a and JFC Windmill^a

Received Date

Accepted Date

DOI: 00.0000/xxxxxxxxxx

A method for predicting the solidification and stress of a digital light processing 3D print process is presented, using a voxel-based, multi-layer model to predict the degree of polymerization of the material at every stage during the print. Additive manufacturing offers extremely short development cycles, making predictive modelling of the complex chemical and mechanical interactions of photopolymerization during part construction unappealing compared to iterative work-flows. Accurate predictions of stress, and the impact of the print parameters and post-print process upon stress, become increasingly important for 3D printing micro-scale electrical and mechanical systems as we design resonators and conductive layers. The process uses a simple method of printed cantilevers to calibrate the stress from various print processes such as propagation of the polymerization front and polymerization gradient. The model is found to have good predictive value and is capable of stress and solidification prediction from a computer aided design file.

1 Introduction

Stereo-lithography and digital light processing (DLP) based processes are well suited to manufacturing complex 3D geometries at small scales^{1,2} with recent work focusing on DLP based microfluidics^{3,4}, MEMS design^{5,6} and sensor technology^{7,8}. Unfortunately at these length scales known issues with residual stress gradients from the polymerization process^{9,10,11} and the intensity distribution from individual pixels of the projected mask image^{12,13} can have a catastrophic effect on a final build. A growing body of work on 4D printing seeks to exploit the effect of polymerization stress at the micro-scale to generate planar to 3D structures^{14,15} or structures made by origami folding^{16,17}.

This work is concerned with the prediction of stresses in DLP prints with a view to reducing the impact of the build parameters on polymerization stress rather than harnessing it. The focus is on suspended structures at the micro-scale such as membranes and resonators since these components are most adversely affected by through thickness layer stress gradients⁷, however the volumetric model presented here is generally applicable to bulk and supported structures. The method takes as its basis the 2D pixel based model of Kang et al.¹² in combination with multi-exposure polymerization process models⁴ to determine the solidification

and degree of polymerization of a 3D printed part, then uses estimations of material properties from the degree of polymerization of a polymer¹⁰ to create a voxel based model of polymerization shrinkage and Young's modulus throughout the part. Calibration of the model is performed by printing a series of test structures, similar to well established techniques such as printing clamped-clamped bridges to obtain resin parameters from print thickness, using cantilevers to estimate through thickness stress from material curvature and calibrating polymer shrinkage parameters for the resin.

For the process described here poly(ethylene glycol) diacrylate (PEGDA) is used as the base resin for all parts due to its common use in the literature and ease of tailoring of the printing parameters allowing for easy comparison to existing studies. When calibrated the combined models predictions of stress and solidification are found to be a good reflection of printed parts, and account for two of the main, non-destructive polymerization shrinkage stresses during printing. The clarification 'non-destructive' is necessary as the model's predictions hold only when the parts are not cleaned using isopropyl alcohol (IPA) – a ubiquitous cleaning method in DLP based additive manufacturing. When suspended structures are cleaned with IPA significant damage and material loss is revealed on partially polymerized areas, leading to extreme curvatures and warping of the printed part. The cleaning process further introduced distinct scarring on the underside of suspended structures and measurable material loss. This destructive process is clear and constant in thin structures, but less distinct in print thicknesses appropriate to 4D printed structures.

^a University of Strathclyde, Centre for Ultrasonic Engineering, Glasgow, UK. Tel: 0141 444 4079; E-mail: andrew.reid@strath.ac.uk

[†] Electronic Supplementary Information (ESI) available: Dataset of cantilever measurements, MATLAB and COMSOL files of voxel based method. See DOI: 10.1039/cXsm00000x/

The motivation behind this paper was to seek reduction and predictability in stresses in micro-scale membranes and resonators, however the 3D solidification and stress models are appropriate for printing micro-channels and voids for microfluidics applications. The reduction of stresses in all cases requires air drying or mechanical cleaning and careful consideration to part orientation and ultra-violet (UV) light intensity.

2 Model setup

2.1 Voxel based solidification

Solidification modelling follows previous work in estimating the degree of conversion of the polymer resin throughout a part from the ultraviolet dose energy¹⁸. The degree of conversion is a representation of the length and distribution of polymer chains. During exposure to UV light the C=C bond of an acrylate are opened and converted to a single bond in a polymer chain¹⁹. While the absolute conversion may be measured from Fourier transform infrared spectroscopy²⁰ here the normalized degree of conversion parameter ϕ is used, $0 < \phi < 1$, with a value of 0 indicating liquid resin and a value of 1 indicating that polymerization has reached its maximum extent^{21 22}. The rate of polymerization in the material on this scale depends on the current level of polymerization at that point $\phi(x, y, z, t)$, the irradiance at that point $I(x, y, z, t)$ and the reaction constant K , which in this model is obtained by curve fitting to measured data.

$$\frac{\partial \phi(x, y, z, t)}{\partial t} = K [1 - \phi(x, y, z, t)] I(x, y, z) \quad (1)$$

The degree of conversion of the material at any given point can then be expressed as:

$$\phi(x, y, z, t) = 1 - e^{-KtI(x, y, z)} \quad (2)$$

Digital light processing uses a digital micro-mirror device to control the pattern of irradiance on the surface of the resin. This digital mask might be considered as an array of pixels with a point spread function. A single pixel distribution would then be

$$I_{px}(x, y) = I_0 e^{-\frac{2r(x, y)^2}{\omega^2}} \quad (3)$$

where I_{px} is the light intensity at co-ordinates x and y from a single pixel with a peak intensity at the centre of I_0 . The function $r(x, y)$ is the distance to the centre of the pixel (x_0, y_0) from (x, y) and ω is the Gaussian half-width of the intensity distribution. In order to obtain a flat-topped distribution, the Gaussian half width of each pixel's distribution will overlap several other pixels²³. A continuous block of pixels is required to obtain an irradiance field which does not vary significantly across the surface of the resin (Figure 1). It is typically this flat-field intensity which is quoted by the manufacture as the field intensity, however for narrow regions and around the edges of builds this assumption will no longer hold.

Calculating the intensity profile on the surface of the polymer simply requires the sum of the intensity distributions from all illuminated pixels, each of which is provided relative to the centre of the pixel.

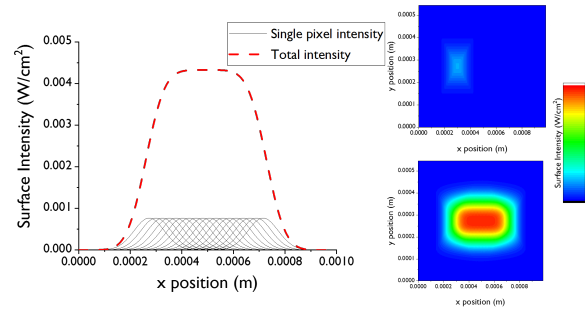


Fig. 1 Illustration of contribution of a single pixel to the irradiance field on the surface of a polymer resin. (Left) The irradiance of each individual pixel is calculated with a Gaussian half width of $106 \mu\text{m}$ and a pixel pitch of $26 \mu\text{m}$. The individual pixel contributions are summed to achieve the final irradiance on the surface. (Right) Colourmap of surface irradiance showing X-Y distribution from a single pixel (top right) and a single row of pixels (bottom right).

$$I_{surf}(x, y) = \sum_i \sum_j I_0 e^{-\frac{2r(x, y)^2}{\omega^2}} \quad (4)$$

Extending to three dimensions uses the surface intensity distribution in equation 4 in combination with the Beer-Lambert law. The parameter μ is the attenuation rate of light through the material, frequently this is described by its reciprocal known as the critical depth³.

$$I(x, y, z) = I_{surf}(x, y) e^{-\mu z}$$

$$I_{surf}(x, y, z) = \sum_i \sum_j I_0 e^{-\frac{2r(x, y)^2}{\omega^2}} e^{-\mu z} \quad (5)$$

During photo-polymerization the transition from liquid to solid is considered to be passed when the degree of conversion ϕ surpasses a critical value ϕ_c which is the gelation point. The solidified thickness may be calculated from the combination of equations 2 and 5.

$$z_p = \ln \left[\frac{KI(x, y, 0)I}{\ln \frac{1}{1-\phi_c}} \right] \frac{1}{\mu} \quad (6)$$

From this, knowing the intensity pattern on the surface of the resin, the parameters K and μ may be evaluated by curve fitting tests builds of single layer suspended structures with varying exposure times.

The preceding steps give the exposure of the polymer for a single layer, however 3D printed structures are fabricated layer-by-layer in multiple exposure steps. As the attenuation of the incident UV light is typically much lower than the thickness of a build layer every printed layer will received further doses as subsequent layers are exposed. A full model must also account for these doses, which can be achieved by successive application of equation 5 for each build layer. If we take the plane $z = 0$ as the exposed surface of the initial build layer, then the irradiance for each exposure step would be:

$$I_n(x, y, z, n) = \sum_n \sum_i \sum_j I_0 e^{\left[\frac{2r(x,y)^2}{\omega^2} \right]} e^{-\mu((n+1)z_{th} - z)} \quad (7)$$

Where z_{th} is the build layer thickness and $(n+1)z_{th}$ is the position of the exposed surface of the n^{th} layer. Only layers preceding the current exposure should receive an additional dose so equation 7 requires a condition so that for any z co-ordinate higher than the top of the current build layer the exposure is zero.

$$I_n(x, y, z, n) = \begin{cases} \sum_n \sum_i \sum_j I_0 e^{\left[\frac{2r(x,y)^2}{\omega^2} \right]} e^{-\mu((n+1)z_{th} - z)}, & \text{for } \frac{z}{z_{th}} \leq n+1 \\ 0 & \text{for } \frac{z}{z_{th}} > n+1 \end{cases} \quad (8)$$

The result is a 3D matrix of the UV light intensity at each point in the material from which we may calculate the dose energy by multiplying by the exposure time, and the degree of conversion at each point.

$$\phi(x, y, z, t) = 1 - e^{-KtI(x,y,z)} \quad (9)$$

Simple scripts can be written to take a computer aided design model file, slice it into a series of 2D bitmap images representing the illuminated pixels, and then build the degree of conversion model layer by layer (Figure 2).

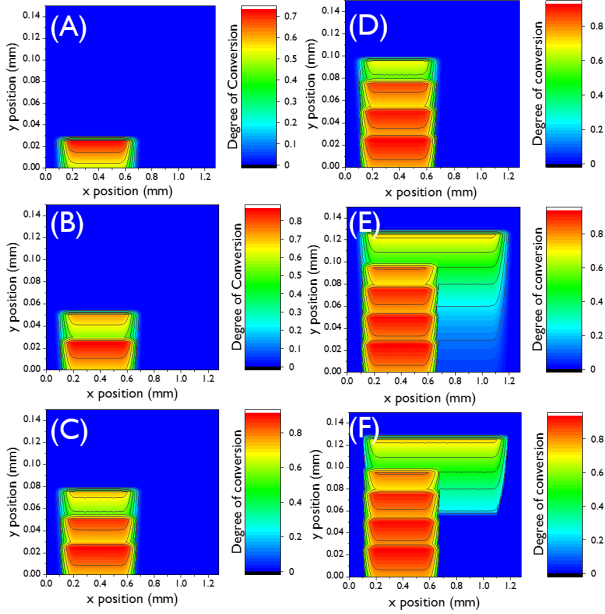


Fig. 2 2D slices of degree of conversion of a polymer showing layer by layer progression of polymerization. In each iteration the energy dose is calculated from the pixel map and Beer-Lambert law, then areas where the degree of conversion falls below the polymerization threshold are set to zero before the next layer is added.

2.2 Stress models

The degree of conversion in PEGDA is related to the Young's modulus by a rate linear model²⁴

$$E(\phi) = E_0(\phi - \phi_c)^{1.8} \quad (10)$$

and to shrinkage strain by a linear function

$$\epsilon^s(\phi) = \epsilon_{initial}^s + (\epsilon_{final}^s - \epsilon_{initial}^s)(\phi - \phi_c). \quad (11)$$

Here E_0 represents a base Young's modulus, and the initial and final subscripts for the strain represent the shrinkage strain at gelation point and for a fully cured material respectively.

Two competing stress fields are considered in this method, both based on the volume shrinkage of the resin as photopolymerization forms covalent bonds between the monomer resin and cross-linking strands. The first is the elastic bi-morph model described and used in 4D printing studies^{25 26}. As a resin layer is exposed to a light source the material closest is polymerized first, with the front of polymerization progressing steadily towards the previous build layer or build plate where it hopefully bonds sufficiently well to withstand separation. The first polymerized material is unconstrained, usually resting on a non-stick surface such as Teflon in the case of bottom-up DLP or supported by liquid resin in the case of top-down DLP, and shrinks freely without stress. Subsequent material is constrained by this solidified region and so as it shrinks as stress field is generated in a manner similar to an elastic bi-morph or shape distortion in stereo-lithographic systems²⁷. This bending may be described by a force equilibrium equation along the thickness direction which varies with time.

$$\int_0^{z(t)} \sigma dz = \int_0^{z(t)} E \epsilon^e dz = 0 \quad (12)$$

$$\int_0^{z(t)} z \sigma dz = \int_0^{z(t)} z E \epsilon^e dz = 0 \quad (13)$$

Here z is the solidified thickness, and ϵ^e represents the total stress on the material which is set to zero if the material is below the polymerization threshold, to $\epsilon^e = \epsilon - \epsilon^s$ as the material is printed (i.e. the polymerization shrinkage ϵ^s is constrained by the build block and base preventing bending), and to be equal to the shrinkage strain when the material is removed from the printing substrate. The integral domain varies with time and may only be solved incrementally by time intervals, however it will be apparent from equation 11 that a significant part of polymerization shrinkage occurs at gelation point meaning the stress gradient in the material is dominated by this initial shrinkage in the first cured material resulting in a boundary layer with a high stress gradient (Figure 3).

In addition to this stress source a second stress is developed in the material through the polymerization gradient through the thickness of a layer as may be seen from the combination of equations 9 and 11. This stress gradient acts in the opposite direction to the stress caused by the movement of the polymerization front and will, temporarily, overwhelm it. The primary reason why this stress is considered temporary is that as material is further cured, either from the printing of subsequent layers or via post-curing, the polymerization gradient would be expected to reduce or be removed entirely. The bending caused by this may therefore only be seen in parts freshly printed and not yet cured or washed, how-

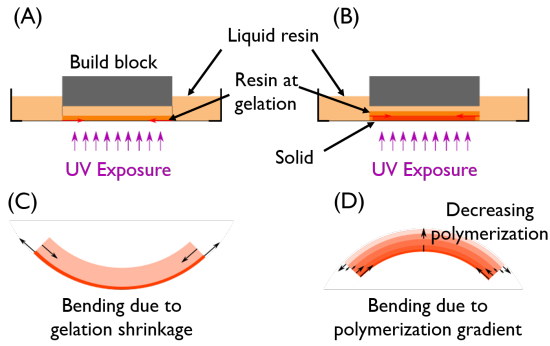


Fig. 3 Illustration of two conflicting sources of stress from printing process. (A) The printing process is bottom up, so material resting on the teflon base reach gelation first and experience the initial shrinkage unconstrained. (B) As the polymerization front progresses the resin reaching gelation point experiences the initial shrinkage constrained by the material that has already reached gelation. (C) Although the progress of the polymerization front is continuous we may model it as a bimorph with a thin boundary layer of initial cured material as the base with the remainder of the layer thickness exerting a compressive stress on it. The centre of bending is away from the light source. (D) The opposite stress is generated by the gradient of polymerization which follows the Beer-Lambert law, in which the direction of bending is towards the light source.

ever for clamped-clamped beams and membranes it may induce significant buckling which is not reversed.

A number of other sources of stress in the print process have been described in the literature, including the separation forces between the print substrate and part²⁸, post-print curing stresses⁹ and stresses induced by surface tension during part cleaning¹⁵. Of these we have not included here the separation forces, which are expected to be related to the mechanical characteristics of the printer rather than the resin, and have attempted to maintain an even post-print cure to show the effect of the reduction of stress from the polymerization gradient. Stresses induced from the IPA washing process appear to have particularly dramatic effects in suspended structures which we describe here but have not included in the model as the effects appear to be caused by material damage.

3 Methods

3.1 3D printed overhangs

Test structures were created using a commercially available 3D printer (Asiga Pico HD) with slicing of CAD models performed by the manufacturer's software (Asiga Composer). The resolution is advertised as $27 \mu\text{m}$ in the x-y plane however this should be considered the pixel pitch. The Gaussian half-width of a single pixel was measured via a CCSD beam profiler and DataRay acquisition software by projecting a single pixel column without build tray or block. The measured half-width of $106.6 \mu\text{m}$ could be combined with the measured flat field intensity of $26.6 \text{mW}/\text{cm}^2$ to calculate the individual pixel centre intensity through equation 3.

All structures presented in this paper were printed using poly(ethylene glycol) diacrylate (PEGDA, MW250), with penylbis(2,4,6-trimethylbenzoyl) phosphine oxide (Irgacure 819) as the photo-initiator. Sudan I was used as an absorber in concen-

trations of 0.2% and 0.4% by weight/weight together with 1% (w/w) Irgacure 819. Preparations were sonicated for 30 min before use and stored in foiled wrapped containers to protect the resins from light.

Values of attenuation and critical dose were fitted from measurements of the printed thickness of clamped beam structures such that

$$z_p = \frac{1}{\mu} \ln D - \frac{1}{\mu} \ln D_c \quad (14)$$

where z_p is the printed height of the crossbar, D is the dose energy at the illuminated surface of the polymer ($D = I(x, y, z)$) and D_c is the minimum irradiance energy required to reach the gelation point. The attenuation μ denotes the inverse of the gradient of the printed height against the natural log of the dose. The polymerization constant K is then taken from equation 2.

Measurements of print thickness were initially made with an external micrometer, and confirmed along with measurements of curvature in images collected with a Leica M-80 stereomicroscope in combination with a Canon DSLR and DigiCam software, with the image analysis performed in ImageJ with the Kappa plug in for curvature analysis^{29 30}. The critical depths and polymerization constant parameter for the two major resin cases are listed in Table 1.

Table 1 Critical depth and polymerization constant parameters estimated from print height along with measured parameters of print hardware

Parameter (units)	0.2% Sudan I	0.4% Sudan I
Critical depth $\frac{1}{\mu}$	$112.4 \mu\text{m}$	$88.03 \mu\text{m}$
Polymerization constant (K)	22.02	7.45
Pixel Half-Width	$116.6 \mu\text{m}$	-
Pixel centre intensity (I_0)	$0.655 \text{mW}/\text{cm}^2$	-

Additional measurements of test structures and of benchmark models were made via X-Ray Computer Tomography using the Bruker Skyscan 1172 with SHT 11 megapixel camera and Mamamatsu 80kV (100 μA) source. No filter was applied to the X-Ray source and a voltage of 45kV was applied for an exposure time of 380ms. The images generated were 2664 x 4000 pixels with a resolution of $2.97 \mu\text{m}$ per pixel. Volumetric reconstruction of the slices was generated by Bruker's CTvol software. The threshold for the attenuation signal was set manually to eliminate speckle around the sample and then further cleaned with a thresholding mask using Bruker's CTAn software. The images produced by the uCT are based on the level of attenuation through the sample which is dependent on the thickness of the material and its absorption coefficient. Two methods were used for cleaning the 3D printed parts: air-drying via high-pressure nozzle and immersion in isopropyl alcohol. Post curing was performed using a custom UV oven with the curing direction kept consistent with the UV direction during print. Parts were cured for 500s to ensure consistent polymerization through the print.

3.2 Voxel based simulation

The model predictions for degree of conversion were primarily coded in MATLAB. CAD files for 3D printed parts were sliced using Autodesk's Netfabb, generating a series of binary images corresponding to the state of each pixel (on/off) in each layer of the printed part. For each print layer the irradiance pattern on the surface of the material corresponding to the pixel pattern was calculated and the cumulative effect on the dose on all preceding layers. Point clouds for the degree of polymerization throughout the model could then be generated from Equation 9. 2D models of individual slices of geometry for plane stress approximation simulations and full 3D models were generated using iso2mesh³¹.

2D and 3D models of the printed parts were then created in COMSOL Multiphysics 5.4 from mesh data exported from MATLAB (Figure 4). Young's modulus throughout the material frame was taken from equation 10 with base value E_0 of $3GPa$ using an interpolation of the degree of polymerization point cloud with the X,Y,Z co-ordinates as arguments. The Poisson's ratio was taken as 0.32 and the material density assumed constant at $1183kg/m^3$. The strain gradient, calculated from the point cloud, was applied as a thermal expansion field similarly interpolated from the voxel model using the rate of volumetric shrinkage by degree of polymerization as the temperature with coefficient of thermal expansion of -1. The polymerization front was simulated as a boundary layer with a fixed volumetric shrinkage of the initial shrinkage at gelation.

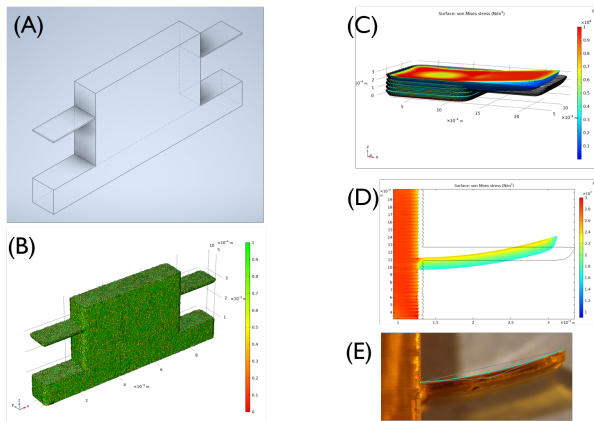


Fig. 4 (A) Test block with two equal 2mm cantilevers generated in CAD. This model is sliced, and the resulting bitmap files used to generate a pixel map which is fed into the voxel model and then to generate an iso-surface mesh at the critical dose threshold (B). (C) A simple cantilever model in 3D shows bending due to the polymerization gradient, however the full CAD model is time consuming to mesh in 3D so plane stress assumptions are used in (D) to create a 2D slice from the voxel model. (E) Shows a printed cantilever at 0.2% Sudan I concentration exposed for 1.6 seconds for comparison to the plane stress model in (D).

In addition to the voxel based model a simplified stress model for the cantilever trails was generated based on rectangular cross sections and plane stress assumptions with the rectangle height determined by equation 6 allowing for quick parametric sweeps of print parameter properties.

4 Results and discussion

The solidification and stress models are first validated by comparison between predicted and modelled cantilever curvatures and thicknesses. Monomer resins with concentrations of Sudan I and 0.2% and 0.4% at exposure times of 0.5s to 16s are further separated according to the post-print treatment. Four sets of measurements and model comparisons are therefore made: for parts cleaned with pressurized air, for parts cleaned via washing in an IPA bath and for both 'green' parts and after 500s exposure in an UV oven. This became necessary once it the radical effect of the IPA wash on both the thickness and the curvature of the cantilevers was appreciated.

The direction and the magnitude of curvature of cantilever deformation could change dramatically with exposure time and cleaning process. Air dried parts would curve downwards at low energy doses, then exhibit a dramatic change in curvature direction at higher exposure times. Parts washed in IPA would curl more dramatically downwards, often deforming into circular forms in thinner cantilevers. The approach of 4D printing treating the stress model as a form of elastic bi-morph caused by the front of polymerization shrinkage may only allow curvature in one direction: with the centre of the radius of curvature on the underside of the part away from the direction of UV exposure. A competing source of stress, acting with the opposite moment, would naturally stem from the gradient of polymerization through the cantilever. This stress would naturally be low at small exposure doses as the illuminated face would not be significantly more polymerized than the underside of the overhanging structure. The stress would then reach a maximum as the illuminated face approached fully cured, as this would be the maximum difference in polymerization through the cantilever, before receding with the increasing thickness of the structure. The superposition of the two competing stress models yields good agreement with measured results in the case of air-dried green parts (Figure 5).

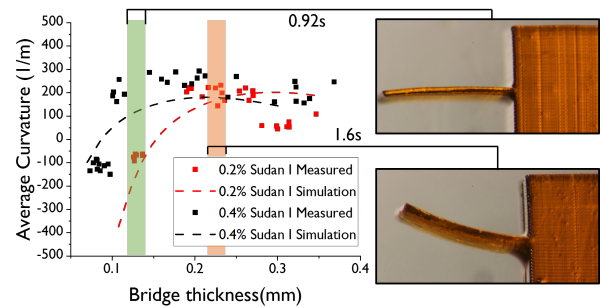


Fig. 5 Comparison of measured curvatures and model for cantilevers that are air dried and 'green' - that is without post-curing. Both the bi-morph effect and the polymerization gradient effect are included in the stress model. In lower exposures (green bar) the bi-morph effect can be seen to dominate and the bending is away from the cure direction, while in higher exposures (orange bar) the polymerization gradient reaches a maximum and overwhelms the stress on the cantilever causing bending in the other direction.

As the air-dried parts are post cured, this second source of stress from the polymerization gradient should diminish as all parts of

the suspended structure approach the same polymerization. This result is observed in Figure 6.

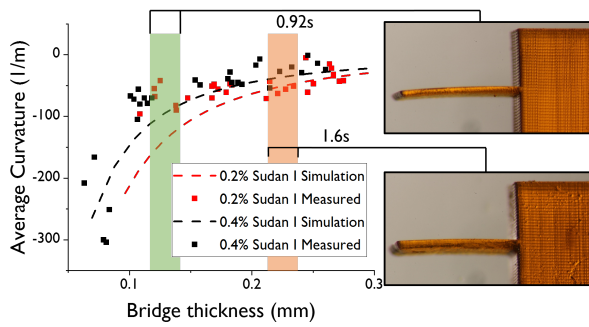


Fig. 6 The same measurement and sample set that were used to generate the previous air dried 'green' results are measured again after post-cure. The polymerization gradient would now be expected to have been eliminated by the post-cure step leaving only the initial stress from the progression of the polymerization front. The lower exposure times were already dominated by the bi-morph effect and show little change, which the higher exposures show the direction of curvature has changed completely as the polymerization gradient is eliminated.

IPA washed parts show extremely large deformations which follow the same direction of moment and exponential decay as the bi-morph model but with curvatures nearly an order of magnitude greater (Figure 7).

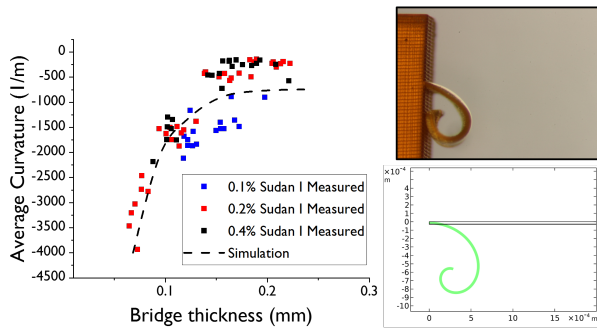


Fig. 7 Parts washed in IPA exhibit extreme curling which is here simulated with an average stress gradient of 9 GPa/m through the thickness of the cantilever. Cantilevers show no sign of stress from polymerization gradient and exhibit no change after post-cure.

Papers commenting on the effect of bending of the IPA have suggested that the capillary action of cleaning and drying samples in IPA when detaching from a substrate may be responsible for inducing some bending stresses. In these experiments the structures are freely suspended, preventing the one sided action seen in¹⁵. Adhesive forces, another suggested influencing factor on bending curvatures and geometries would be expected to be the same in both cleaning methods. Parts washed in IPA immediately after printing exhibited noticeable thinning of the cantilever, with accompanying scoring visible on the underside in X-Ray CT scans of the printed part (Figure 8). This seems more indicative of material loss or material damage from the washing process, either through straight dissolution of partially polymerized material or damage from cracking during swelling and desiccation of the

green part. Post curing of structures cleaned in IPA did not result in any change in curvature. Due to the ubiquity of IPA washing in 4D printing papers it is difficult to find any comparison between IPA washed and non-IPA washed models of polymerization stress.

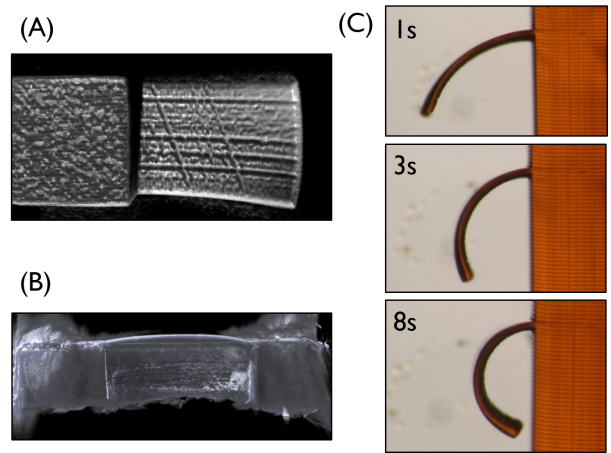


Fig. 8 (A) X-Ray CT image showing scoring and material loss on the underside of a cantilever. (B) The same effect causing buckling in a clamped membrane (C) When removed from IPA cleaning, cantilevers deform rapidly with no outside input as material dries.

The models presented here have been small volume, as the focus has been on stress in micro-structures, however the method is capable of estimating solidification and stress in bulk models. Due to the poor scaling of voxel based methods, models approaching the maximum build volume of a DLP system must be reconstructed as a series of z-slices of degree of conversion to allow them to be solved at a reasonable resolution. Z-slices are sequentially calculated and summed to produce a complete volumetric reconstruction. Standard 3D print 'stress tests' such as the Benchy 3D model or medieval castle (Figure 9) could be modelled at a voxel resolution of 10 μ m using this method.

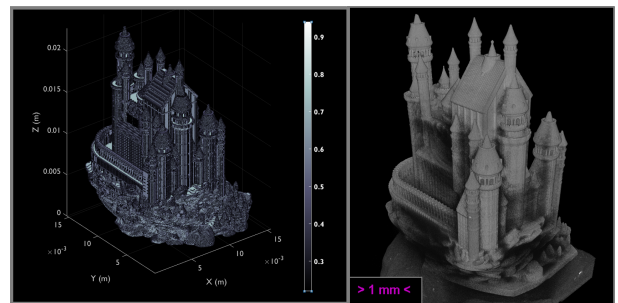


Fig. 9 Comparison of estimated degree of conversion of a large scale model (here a standard test-print of a medieval castle, left) with X-Ray CT image of 3D printed part (right). The model is generated to illustrate the ability of the method to be applied to larger models, the image left has a voxel resolution of 10 μ m, for a model size of 15x15x20mm outputting a 445Mb point cloud in 36 minutes.

5 Conclusions

The method here allows prediction and calibration of two primary non-destructive stress sources in multi-layer 3D prints. 3D models

of solidification are used here to demonstrate the stress modelling technique in membranes, but have clearer applications in printing voids and micro-channels for microfluidic applications. Washing suspended structures in IPA appears to have a destructive effect on partially polymerized regions, which is readily apparent in extremely thin suspended structures. The impact of the washing stage on 4D printing techniques is difficult to quantify from the literature as the process step is standard and there is therefore no control group to compare stress against.

Conflicts of interest

There are no conflicts to declare.

Acknowledgements

The work was funded by a Leverhulme Trust Early Career Fellowship ECS-2019-185 and the European Research Council under the European Union's Horizon 2020 research and innovation program (grant agreement no. 812938).

Notes and references

- 1 A. Bertsch, J. Jézéquel and J. André, *Journal of Photochemistry and Photobiology A: Chemistry*, 1997, **107**, 275–281.
- 2 C. Sun, N. Fang, D. Wu and X. Zhang, *Sensors and Actuators A: Physical*, 2005, **121**, 113–120.
- 3 H. Gong, M. Beauchamp, S. Perry, A. T. Woolley and G. P. Nordin, *RSC advances*, 2015, **5**, 106621–106632.
- 4 H. Gong, B. P. Bickham, A. T. Woolley and G. P. Nordin, *Lab on a Chip*, 2017, **17**, 2899–2909.
- 5 E. Cesewski, A. P. Haring, Y. Tong, M. Singh, R. Thakur, S. Laheri, K. A. Read, M. D. Powell, K. J. Oestreich and B. N. Johnson, *Lab on a Chip*, 2018, **18**, 2087–2098.
- 6 O. Ulkir, *Materials Research Express*, 2020, **7**, 075015.
- 7 B. Tiller, A. Reid, B. Zhu, J. Guerreiro, R. Domingo-Roca, J. C. Jackson and J. Windmill, *Materials Design*, 2019, **165**, 107593.
- 8 Z. Zhu, H. S. Park and M. C. McAlpine, *Science advances*, 2020, **6**, eaba5575.
- 9 D. Wu, Z. Zhao, Q. Zhang, H. J. Qi and D. Fang, *Soft matter*, 2019, **15**, 6151–6159.
- 10 J. Wu, Z. Zhao, C. M. Hamel, X. Mu, X. Kuang, Z. Guo and H. J. Qi, *Journal of the Mechanics and Physics of Solids*, 2018, **112**, 25–49.
- 11 P. Bychkov, V. Kozintsev, A. Manzhurov and A. Popov, *Mechanics of Solids*, 2017, **52**, 524–529.
- 12 H.-W. Kang, J. H. Park and D.-W. Cho, *Sensors and Actuators A: Physical*, 2012, **178**, 223–229.
- 13 Y. Li, Q. Mao, X. Li, J. Yin, Y. Wang, J. Fu and Y. Huang, *Additive Manufacturing*, 2019, **30**, 100889.
- 14 C. A. Spiegel, M. Hippler, A. Münchinger, M. Bastmeyer, C. Barner-Kowollik, M. Wegener and E. Blasco, *Advanced Functional Materials*, 2019, 1907615.
- 15 A. A. Bauhofer, S. Krödel, J. Rys, O. R. Bilal, A. Constantinescu and C. Daraio, *Advanced Materials*, 2017, **29**, 1703024.
- 16 G. Liu, Y. Zhao, G. Wu and J. Lu, *Science advances*, 2018, **4**, eaat0641.
- 17 L. S. Novelino, Q. Ze, S. Wu, G. H. Paulino and R. Zhao, *Proceedings of the National Academy of Sciences*, 2020, **117**, 24096–24101.
- 18 J. Wu, *Thesis*, 2018.
- 19 T. Y. Lee, T. M. Roper, E. S. Jonsson, I. Kudyakov, K. Viswanathan, C. Nason, C. Guymon and C. E. Hoyle, *Polymer*, 2003, **44**, 2859–2865.
- 20 M. Martin-Gallego, R. Verdejo, M. A. López-Manchado and M. Sangermano, *Polymer*, 2011, **52**, 4664–4669.
- 21 J. T. Cabral, S. D. Hudson, C. Harrison and J. F. Douglas, *Langmuir*, 2004, **20**, 10020–10029.
- 22 A. Vitale and J. T. Cabral, *Materials*, 2016, **9**, 760.
- 23 C. Zhou and Y. Chen, *Proceedings of Solid Freeform Fabrication Symposium*, Austin, Texas, 2009.
- 24 Z. Zhao, J. Wu, X. Mu, H. Chen, H. J. Qi and D. Fang, *Science advances*, 2017, **3**, e1602326.
- 25 T. van Manen, S. Janbaz and A. A. Zadpoor, *Materials Today*, 2018, **21**, 144–163.
- 26 X. Kuang, J. Wu, K. Chen, Z. Zhao, Z. Ding, F. Hu, D. Fang and H. J. Qi, *Science advances*, 2019, **5**, eaav5790.
- 27 Y.-M. Huang and C.-P. Jiang, *The International Journal of Advanced Manufacturing Technology*, 2003, **21**, 586–595.
- 28 O. Santoliquido, P. Colombo and A. Ortona, *Journal of the European Ceramic Society*, 2019, **39**, 2140–2148.
- 29 H. Mary and G. Brouhard, *BioRxiv*, 2019, 852772.
- 30 J. Schindelin, I. Arganda-Carreras, E. Frise, V. Kaynig, M. Longair, T. Pietzsch, S. Preibisch, C. Rueden, S. Saalfeld and B. Schmid, *Nature methods*, 2012, **9**, 676–682.
- 31 Q. Fang and D. Boas, *línea*. Disponible en: <http://iso2mesh.sourceforge.net/cgi-bin/index.cgi>, 2010.